CrossMark

ORIGINAL PAPER

Smart, lightweight, flexible NiO/poly(vinylidene flouride) nanocomposites film with significantly enhanced dielectric, piezoelectric and EMI shielding properties

Biplab Dutta[1] · Navonil Bose[2] · Epsita Kar[1] · Sukhen Das[3] · Sampad Mukherjee[1]

Abstract We report a facile technique to fabricate flexible and self-standing NiO/PVDF nanocomposite films. Detail structural and thermal characterizations of nanocomposite films show the gradual increase of electroactive β-phase of PVDF with increasing NiO nanoparticles content. The enhancement of β phase in the NiO/PVDF nanocomposites has been explained from physicochemical point of view. Electrical properties of the nanocomposites indicate fair improvement in dielectric properties at low filler loading with less dielectric loss. The value of dielectric constant of 0.75 wt% NiO/PVDF films at 100 Hz is five times higher than that of neat PVDF. Series-parallel model was used to describe the filler concentration dependence of the dielectric constant of the nanocomposites. These nanocomposites also exhibit excellent ferroelectric properties. Nanocomposite films having thickness 300 μm were also successfully employed for microwave shielding application. This work suggests that these films would be very useful for thinner, lighter energy harvesting storage and EMI shielding applications.

✉ Navonil Bose
navonil05@gmail.com

✉ Sampad Mukherjee
smukherjee.besu@gmail.com

[1] Department of Physics, Indian Institute of Engineering Science and Technology, Shibpur, Howrah 711103, India

[2] Department of Physics, Supreme Knowledge Foundation Group of Institutions, Mankundu, Hooghly 712139, India

[3] Department of Physics, Jadavpur University, Kolkata 700032, India

Introduction

Recent research works on conducting filler loaded polymer composites are being concentrated on the solution of two major problems of the modern world: energy harvesting and microwave shielding [1–6]. Regarding the choice of polymers, much attention has been paid on electroactive polymers, particularly on Poly(vinylidene fluoride) (PVDF) and its copolymers due to their high dielectric constant, excellent piezoelectric, pyroelectric and ferroelectric properties [7–10]. These unique features of PVDF results in a wide range of applications in energy harvesting, sensors, actuators, electrostriction for artificial muscles, magneto-striction, non-volatile memories in microelectronics, thin film transistors, pulsed laser, microwave absorbing materials [11–18]. Being a good piezoelectric material, PVDF composites can be used for the conversion of ambient mechanical energy to electrical energy [19], thus can be efficiently use in energy harvesting applications. Among the five different phases, polar β phase of PVDF is mostly responsible for its better piezoelectric, ferroelectric and pyroelectric properties due to its orthorhombic unit cell structure with 'TTT' (all trans) conformation [20]. As a consequence, numerous methods have been developed to enhance the β phase content in PVDF matrix. Different micro-fillers such as $BaTiO_3$ [21], hydrate ionic salts [22], clays [23], rare earth salts [24] are being loaded in the PVDF matrix to enhance the β phase fraction as well as the dielectric properties. Nanofillers [20–26] are also added in PVDF to improve the β phase fraction and dielectric properties. It is well known that usage of metal and metal oxide nanoparticles can significantly improve mechanical, electrical and magnetic properties of polymeric composite films without sacrificing the flexibility of the composite films [20, 26, 27]. Amongst the different metal oxides nanofillers, nickel oxide nanofillers has achieved great importance due to its key role on the enhancement of the electrical properties of polymer composites, however, their possibility in

enhancement of dielectric, ferroelectric and piezoelectric properties have been rarely examined. Thus it will be interesting to study the effect of the nickel oxide nanoparticles (NONPs) incorporation on the nucleation of the electroactive β phase in PVDF as well as to study the structural, thermal, dielectric and ferroelectric properties of the nickel oxide/PVDF nanocomposite films. Recently conductive polymer nanocomposites are frequently used as electromagnetic interference (EMI) shield where various filler materials including metal, metal oxide, clays, ceramics, semiconductor oxide, carbon nanotubes, graphene, inorganic salts, and ferrites are used as fillers [1–6]. Any modern smaller and smarter electronics device for personal, industrial and military applications, which transmits, distributes or uses electrical energy, creates electromagnetic interference. Accordingly EMI shielding materials are urgently required to prevent detrimental impacts of EMI on device performance and human health. Previously Ni/Ferrite/PVDF [5] and Ni/PVDF [1] were used in EMI shielding applications. Thus it will be productive to develop NONPs loaded PVDF nanocomposites for EMI shielding applications.

This present work deals with the development of NiO nanoparticles incorporated PVDF films which have versatile applications in dielectric, piezoelectric ferroelectric and also EMI shielding applications. Hydrothermally synthesized nickel oxide nanoparticles were incorporated in the PVDF matrix. Detailed analyses of the structural and thermal properties of the NONPs loaded PVDF films have been included in this study. Significant improvement of the electroactive β phase nucleation with incorporation of NONPs in PVDF has been explained from the physicochemical point of view. The dielectric, ferroelectric and EMI shielding properties of NONPs/PVDF nanocomposites were also studied in details.

Experimental

Materials

Poly(vinylidene fluoride) (PVDF) pallets ($M_w = 27,500$ g mol^{-1}) were obtained from Sigma Aldrich, USA. Dry N,N,dimethylformamide (DMF; Merck, India), Nickel Chloride Hexahydrate ($NiCl_2$, $6H_2O$, $M_w = 237.69$ g mol^{-1}; Merck, India), Sodium Hydroxide (NaOH; Merck, India) and Ethyl Alcohol (C_2H_6O; Merck, India) were used in this work. All the materials were used in the experiments without further purification.

Synthesis of nickel oxide nanoparticles

The nickel oxide nanoparticles were synthesized using hydrothermal method [28]. In this hydrothermal method, initially 0.1 M solution of $NiCl_2$, $6H_2O$ was prepared in distilled water, then 1 M NaOH solution was added drop by drop to the prior

solution under strong stirring untill the pH of the solution became 12. Afterwards the solution was transferred to a stainless steel autoclave and sealed properly. The autoclave was heated in a furnace at temperature of $200^{\circ}C$ for 24 h. Hence the autoclave was set for natural cooling. After cooling down to room temperature (30 °C), the solution was taken out from the autoclave and centrifuged (3500 rpm) for 20 min. To remove the residual impurities from the as obtained product, it was properly washed for several times using distilled water and ethyl alcohol. The solution was dried to obtain the resultant powder and the powder sample was then calcinated at 400 °C for 4 h. Finally the calcinated powder sample was kept in a vacuum desiccator.

Fabrication of nickel oxide loaded PVDF nanocomposite films

The nickel oxide nanoparticles incorporated PVDF films were fabricated by the simple solution casting method. In the synthesis procedure, at first 500 g of PVDF was dissolved in 10 ml DMF by magnetic stirring at 60 °C. Thereby a certain weight percent (0.25–1 wt%) of the hydrothermally synthesized nickel oxide nanoparticles were added to the solution of PVDF and strongly stirred for 16 h. To obtain a homogeneous mixture, resultant solution was sonicated for 30 min. Finally the nanocomposite films were prepared by casting the mixture in a Petri dish and the mixture was heated at $90^{\circ}C$ till the solvent was evaporated. Neat PVDF films were also prepared by following the same procedure. The details of the synthesized samples are given in the Table 1.

Characterization

To study the structural properties of the synthesized NONPs and nanocomposite films X-ray diffractometer (Bruker-D8) with Cu-Kα radiation (wavelength $1.541A^0$ using Bragg-Brentano goniometer geometry and θ-2θ mechanism) was used. The XRD histograms of all the samples were recorded with a scan speed of 0.01 s per step with 2θ varying from 10 to 50^0 under an operating voltage of 40 kV. Absorption spectra of the as synthesized NONPs and NONPs loaded PVDF films were recorded by

Table 1 Details of the composition of the as synthesized PVDF nanocomposite films

Name of the sample	Percentage of nickel oxide nanoparticles (weight %)
P0	0
PNO0.25	0.25
PNO0.5	0.5
PNO0.75	0.75
PNO1	1

using UV-Visible spectrophotometer (Jasco V-630 Spectrophotometer) in the wavelength ranging from 200 to 1100 nm. Field emission scanning electron microscopy (FESEM) (Quanta FEG 250) was used to study the surface morphology of the as synthesized nickel oxide nanoparticles loaded PVDF films. Energy dispersive X-ray spectroscopy (EDAX) of the samples were also carried out by the same instrument. Structure, shape and size distribution of the nickel oxide nanoparticles were studied by transmission electron microscope (TEM) using FEI.TECHNAI.T-20 G2 SUPERTWIN (200 kV) instrument. Fourier transform infrared (FTIR) spectroscope (Jasco FT/IR-460 PLUS) having resolution of 1 cm^{-1} was used to record the vibrational spectra for all the samples at room temperature. The β phase fraction F(β) in the nanocomposite films were calculated from the FTIR spectra by using the Lambert-Beer Law as follows [29],

$$F(\beta) = \frac{A_\beta}{\left(\frac{K_\beta}{K_\alpha}\right)A_\alpha + A_\beta} \qquad (1)$$

Where A_α and A_β are the absorbance at 764 cm^{-1} and 840 cm^{-1} respectively. K_α(6.1 × 10^4 cm^2 mol^{-1} and K_β(7.7 × 10^4 cm^2 mol^{-1}) are the absorption coefficients at 764 cm^{-1} and 840 cm^{-1} respectively. To study the thermal properties of the samples, differential thermal analysis (DTA) and thermogravimetric analysis (TGA) were performed by using TGA/SDTA851 Mettler Toledo apparatus in air atmosphere at a heating rate 10 °C/min. Differential scanning calorimeter (DSC-60, Shimadzu (Asia Pacific) Pte. Ltd., Singapore) were used to study the crystallization and melting behavior of the neat as well as nanocomposite films. During DSC analysis all the samples were heated from 30 °C to 200 °C at a rate of 10 °C/min in a nitrogen gas atmosphere. Degree of crystallinity (X_c) of the samples were calculated by using the following Eq. [20]:

$$X_c = \Delta H_c / \Delta H_{100\%} \qquad (2)$$

Where, ΔH_c is the enthalpy of crystallization and $\Delta H_{100\%}$ is the melting enthalpy of 100% crystalline PVDF with a value of 104.6 Jg^{-1}. The dielectric properties of the neat and nanocomposite films were studied using a digital LCR meter (Agilent, E4980A). The values of the dielectric constant (ε′), dielectric loss (ε″) and ac conductivity (σ_{ac}) of the samples were calculated from the obtained value of the capacitance and tanδ by using the following equations:

$$\varepsilon' = \frac{C.d}{\varepsilon_\circ A} \qquad (3)$$

$$\varepsilon'' = \tan\delta . \varepsilon' \qquad (4)$$

$$and \ \sigma_{ac} = 2\pi f \varepsilon_\circ \varepsilon'' \qquad (5)$$

where C, d and A are the capacitance, thickness and effective area of the samples respectively. $\varepsilon_\circ$ is the free space permittivity

(8.854 × 10^{-12} F m^{-1}) and f is the frequency of the electric field applied across the samples. The dielectric constant of NONPs pallet was measured using silver as electrodes (area ~ 1cm^2). The P-E hysteresis loops for the samples were measured using Precision LC II ferroelectric tester, Radiant Technologies. Rectangular films of thickness about 300 μm, were used for microwave measurements by the waveguide method in the X band (8.2–12.4 GHz). The samples were inserted into the waveguide coupled to a vector network analyzer (Agilent E5071C) and S-parameters (S$_{11}$ and S$_{21}$) were measured.

Result and discussion

Nickel oxide nanoparticles

X-ray diffraction analysis (XRD) Fig. 1 shows the X-ray diffraction (XRD) pattern of the hydrothermally synthesized nickel oxide nanoparticles, which confirms the well crystalline nature of the sample. The diffraction peaks positioned at 2θ values 37.03°, 43.16°, 62.71°, 75.19°, 79.3° are indexed to the (101), (012), (110), (113) and (202) planes of the crystalline phase of rhombohedral nickel oxide (NiO) (a = 2.955 Å, c = 7.2275 Å) in accordance with the JCPDS no. 44–1159.

Electron microscopy analyses The transmission electron microscopic (TEM) image of the hydrothermally synthesized nickel oxide nanoparticles is shown in Fig. 2a. Inset of the figure shows the size distribution curve of the synthesized nanoparticles as obtained from the TEM micrograph. The figure shows that the nickel oxide nanoparticles possess hexagonal structure with well-defined boundaries. As seen from the size distribution curve the average size of the nanoparticles is
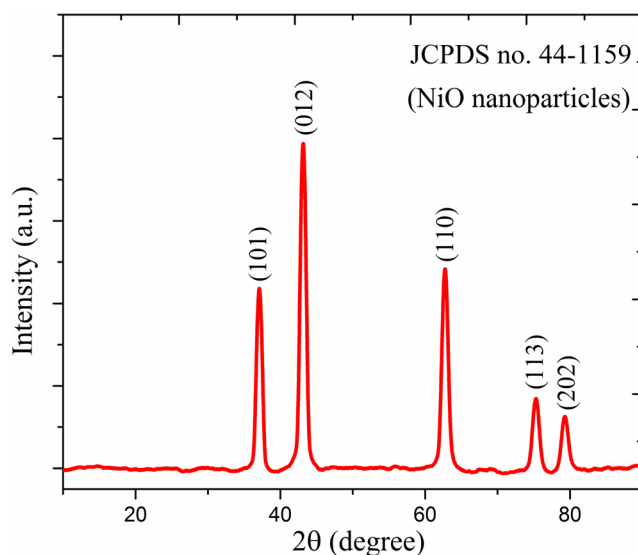

Fig. 1 X-ray diffraction pattern of the hydrothermally synthesized nickel oxide nanoparticles
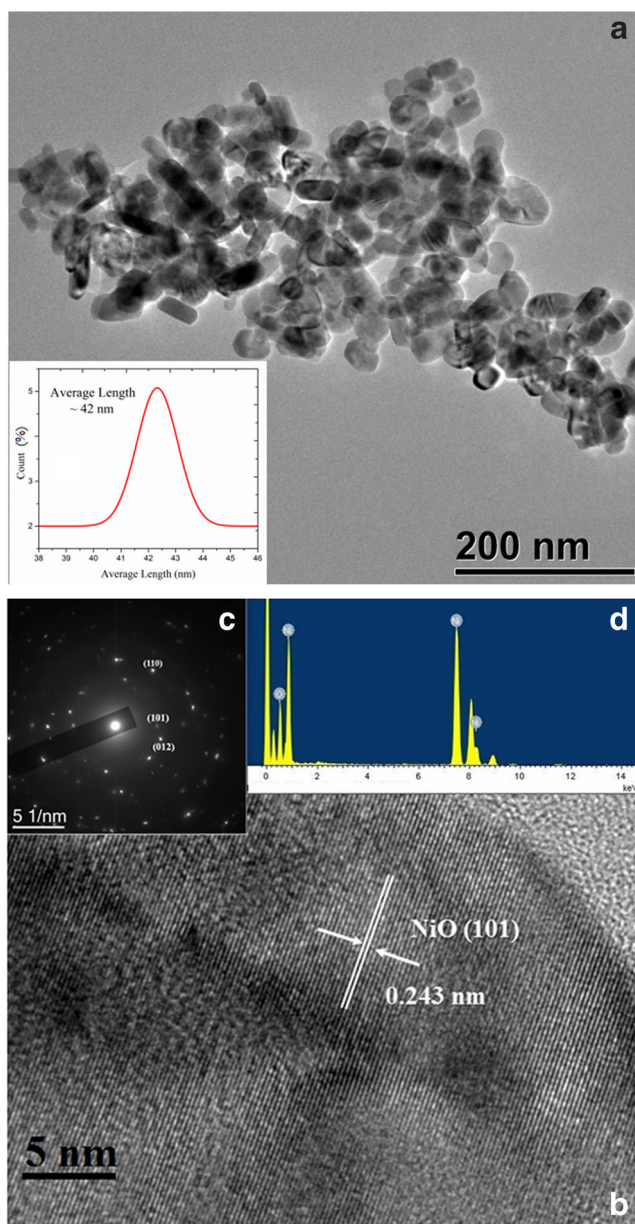
Fig. 2 (a) TEM image of the synthesized nickel oxide nanoparticles. Inset shows the size distribution curve of the nickel oxide nanoparticles; (b) lattice-resolved HRTEM micrograph of the nickel oxide nanoparticles (c) SAED pattern of the synthesized nickel oxide nanoparticles; (d) EDAX result of the as synthesized nickel oxide nanoparticles

~ 44 nm. Figure 2b represents the lattice-resolved high resolution TEM micrograph of NiO nanoparticles which shows the (101) crystal plane with lattice spacing 0.243 nm. Fig. 2c exhibits the selected area electron diffraction (SAED) pattern of nickel oxide nanoparticles. The 'Dot' patterned SAED result depicts the single crystalline nature of the nanoparticles. The d-spacing values, as obtained from the SAED pattern are 2.423 nm, 2.096 nm and 1.483 nm corresponding to the (101), (012) and (110) planes of NiO crystals (JCPDS no. 44–1159) respectively. Fig. 2d shows the EDAX result of the hydrothermally synthesized sample, which depicts only presence of the

characteristic peaks corresponding to the O and Ni elements. This result confirms the high purity of the synthesized nickel oxide nanoparticles.

UV-visible spectroscopy Fig. 3 shows the UV-Visible absorption spectrum of the synthesized nickel oxide nanoparticles. A strong absorption peak positioned at wavelength 310 nm is observed which can be attributed to the nickel oxide nanoparticles. Existence of similar absorption peak for nickel oxide nanoparticles has been already reported by M. Salavati-Niasari et al. [30].

Nickel oxide loaded PVDF nanocomposite films

X-ray diffraction analysis (XRD) To study the polymorphism of neat PVDF and nickel oxide nanoparticles loaded PVDF films X-ray diffraction (XRD) spectroscopy was used. Fig. 4a shows the XRD pattern of the neat PVDF (P0) and NONPs loaded PVDF nanocomposite films (PNO0.25, PNO0.5, PNO0.75 and PNO1). The diffraction pattern of the neat PVDF (P0) infers the semi-crystalline nature of the polymer. The peaks positioned at 2θ values 17.5° (100), 18.2° (020), 19.7° (021), and 26.6° ((201), (310)) of the neat PVDF can be attributed to the nonpolar α phase of PVDF [20, 29]. Two well recognizable peak for the NONPs loaded PVDF films positioned at 2θ values of 36.95° (101) and 43.02° (012) can be clearly indexed to the rhombohedral NiO (JCPDS no. 44–1159), which confirms the presence of the NONPs in the PVDF matrix. It can also be seen from the XRD patterns that with increasing loading fraction of nickel oxide nanoparticles the relative intensity of the peaks corresponding to the α phase of PVDF (positioned at 17.5°, 18.2°, 19.7° and 26.6°) decreases prominently. However for the loaded PVDF films a new peak appears at 2θ values of 20.3° ((020, 101)) which can be attributed to the characteristic peak of β phase of PVDF [20]. This phenomena infers that the loading of the nickel
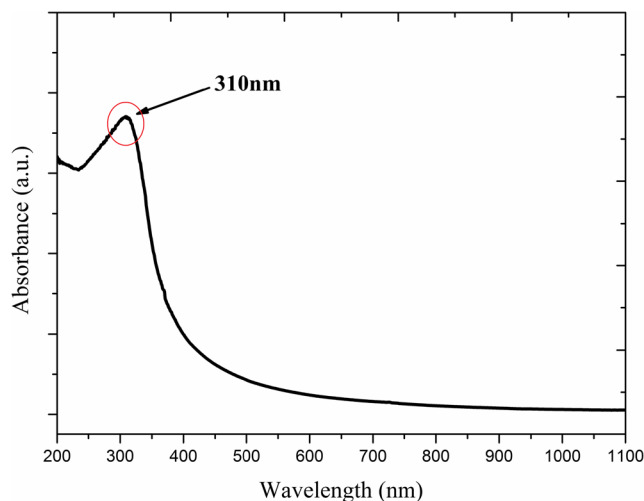
Fig. 3 UV-Visible absorption spectrum of the synthesized nickel oxide nanoparticles
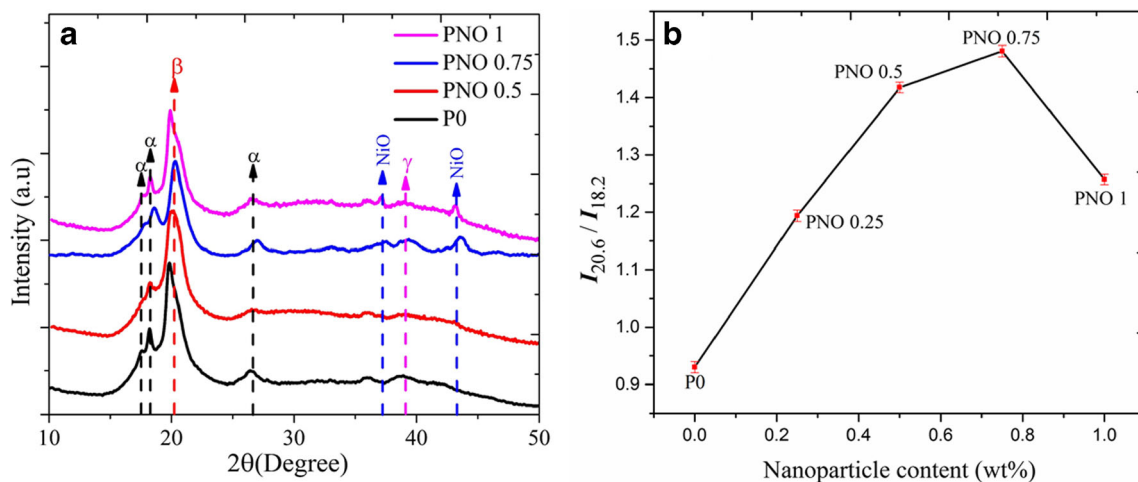
Fig. 4 (**a**) X-ray diffraction patterns of the neat PVDF (P0) and NONPs loaded PVDF films (PNO 0.5, PNO 0.75, PNO 1); (**b**) Ratio of intensities at 20.6° and 18.2° of the samples P0, PNO 0.25, PNO 0.5, PNO 0.75, PNO 1

oxide nanoparticles in the PVDF matrix causes transformation from the nonpolar α phase to polar β phase of PVDF [20, 29]. A closer observation to the figure reveals that the relative intensity of the peaks corresponding to the nonpolar α phase decrease upto 0.75 wt% loading of nanofiller in PVDF matrix, after this critical filler loading the relative intensity of those peaks are increased. This phenomena has occurred may be due to the agglomeration of the nickel oxide nanoparticles in the PVDF matrix. The XRD pattern also shows a peak positioned at 2θ value of 38.9° (211) corresponding to the γ phase of PVDF [20, 29]. This peak is present in the neat as well as loaded PVDF films. Fig. 4b shows the content dependence of the ratio of intensities of the peaks positioned at 20.3° (characteristic peak for β phase) and 18.2° (characteristic peak for α phase). This ratio ($I_{20.3°}/I_{18.2°}$) reflects the β and α phase fraction in the NONPs loaded nanocomposite films. The ratio is about 0.93 for the neat PVDF film and this ratio is increased with the increasing loading fraction of the NONPs in the PVDF matrix. The maximum value of this ratio is achieved for the sample PNO0.75 (0.75 wt%), which is about 1.5. Hence the XRD patterns of the nanocomposite films confirm that the incorporation of the NONPs upto 0.75 wt% leads to the successful phase transformation from the nonpolar α phase to the polar β phases of PVDF.

Field emission scanning electron microscopy (FESEM)
Fig. 5a shows the FESEM micrograph of neat PVDF. The micrograph shows that the matrix of the neat PVDF possesses a highly compact and uniform morphology with a well-recognizable (marked by red circle) spherulite with a diameter about 8 μm. In Fig. 5b, surface morphology of the sample PNO0.75 shows a uniform distribution of the spherulites (marked as red circles in the figure) having average diameter about 2 μm throughout the entire surface of the composite film. These uniformly distributed spherulites confirms the homogeneous dispersion of nickel oxide nanoparticles in the

PVDF matrix for the sample PNO0.75. The size of the spherulites for the sample PNO0.75 is much smaller than the neat PVDF which describes the faster nucleation kinetics in NONPs/PVDF composite films [31]. The NONPs acted as nucleation centers in PVDF matrix, resulting the enhancement of the β phase fraction of the nanocomposite films as well as faster nucleation kinetics. Fig. 5c shows the FESEM micrograph of the PNO1 nanocomposite film, which reveals that the average size of the spherulite (marked by red circle) is increased and it is about 6 μm. This increment occured may be due to the agglomeration of the nickel oxide nanoparticles in the PVDF matrix. Hence the FESEM images supports the enhancement of the electroactive β phase due to the incorporation of the NONPs which is in accordance with the X-ray diffraction result. Inset of the Fig. 5b and c shows the EDAX result of the NONPs loaded PVDF films. These figures show that the characteristic peaks arise only for O and Ni along with the peaks corresponding to the polymeric components C and F of PVDF matrix. Hence the EDAX results confirm the presence of the nickel oxide nanoparticles in PVDF.

UV-visible spectroscopy UV-Visible absorbance spectra of the neat PVDF and NONPs loaded PVDF films (PNO0.25, PNO0.5, PNO0.75 and PNO1) within the wavelength range 200–1100 nm are shown in Fig. 6. It is evident from the figure that there is no absorbance peak for the neat PVDF but for all the NONPs loaded PVDF films there exists a well-defined absorption peak positioned at ~317 nm corresponding to the NONPs. As seen from the Fig. 3, the absorption peak for the NONPs is positioned at wavelength ~310 nm. Hence the absorption peak of the NONPs is shifted by 7 nm in the presence of host polymer matrix. The electronic transition between valence band and conduction band in NONPs may be affected due to the strong electrostatic interaction between the NONPs filler and polymer matrix [20].
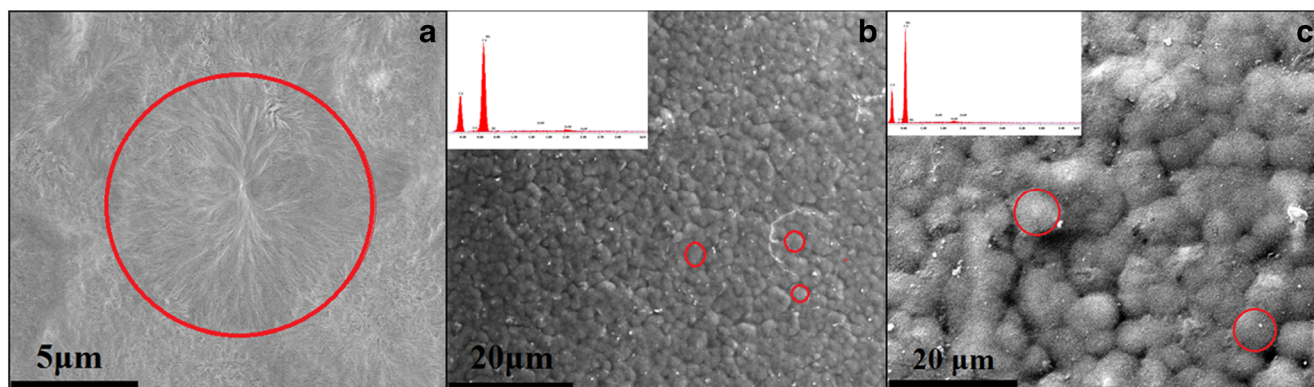
Fig. 5 FESEM micrograph of the (**a**) neat PVDF (**b**) PNO0.75 (**c**) PNO1. Inset shows the EDAX result of the nanocomposite films. Red circle shows the spherulite

Fourier transform infrared spectroscopy Fig. 7a shows the Fourier transform infrared (FTIR) absorption spectra of neat PVDF and NONPs loaded PVDF films (PNO0.25, PNO0.5, PNO0.75 and PNO1). The FTIR spectrum of the neat PVDF shows characteristic peaks positioned at 488 cm^{-1}(CF_2 waging), 532 cm^{-1}(CF_2 bending), 615 cm^{-1} and 764 cm^{-1} (CF_2 bending and skeletal bending), 796 cm^{-1} and 976 cm^{-1} (CH_2 rocking) assigned to the IR bands of nonpolar α phase of PVDF [20, 29] and also two small peaks positioned at 510 cm^{-1}(CF_2 stretching) and 840 cm^{-1}(CH_2 rocking, CF_2 stretching and skeletal C–C stretching) conforming the presence of β phase of PVDF [20, 29]. Figure shows that the relative intensity of the characteristic absorption bands corresponding to nonpolar α phase of PVDF are gradually decreased with increasing NONPs content in PVDF matrix. It can be clearly seen from the figure that for the sample PNO0.75, all the peaks corresponding to α phase are almost completely disappeared, only the characteristic peaks assigned to polar β phase appear prominently at 510 cm^{-1} (CF_2 stretching), 600 cm^{-1} (CF_2 waging), 840 cm^{-1} (CH_2 rocking,

CF_2 stretching and skeletal C-C stretching) [20, 29]. Hence, the FTIR results indicate that significant α to β phase transformation of PVDF is occurred with the loading of the NONPs in the PVDF matrix. β phase fraction (F(β)) is calculated for the nanocomposite films using Eq. (1) to quantitatively study the phase transformation for the NONPs loaded PVDF films. Fig. 7b shows the variation of F(β) with NONPs loading in PVDF matrix. From this figure it can be seen that with the increasing loading fraction the F(β) increases and the maximum value of F(β) c.a. 85% is achieved for 0.75 wt% NONPs loading. The interaction between the filler and the polymer matrix leads to this enhancement of β phase fraction with the filler loading. When the filler content is low the effective interfacial area between the polymer and the NONPs is less, with the increment of the loading of homogeneously dispersed NONPs in the polymer matrix the interfacial area increases. Hence the number of aligned chains having 'all trans' conformation increases and leads to the successful increment of the β phase fraction. However for PNO1 the β phase is reduced. This phenomena may be occurred due to the movement restriction of elongation of the polymer chains in 'all trans' conformation for further loading of the nanofillers, which in turns reduces the β phase content [20].

Thermal analyses Thermal properties of the neat PVDF and NONPs loaded PVDF films have been studied by TG-DTA and DSC techniques. DTA results of the neat PVDF and PVDF nanocomposite films within the temperature range 30 °C to 600 °C are shown Fig. 8a. The enlarged view of the DTA result within the temperature range 100 °C to 200 °C is shown in the inset of the Fig. 8a. The figure shows an endothermic peak positioned around 155.5 °C for the neat PVDF, which is attributed to the melting temperature of the neat PVDF [20, 26]. Fig. 8a also gives a clear evidence that with the increasing loading fraction of the nanofillers (NONPs) the melting temperature of the composite films is increased in comparison to that of the neat PVDF film. A 6° shifting of the melting temperature towards higher
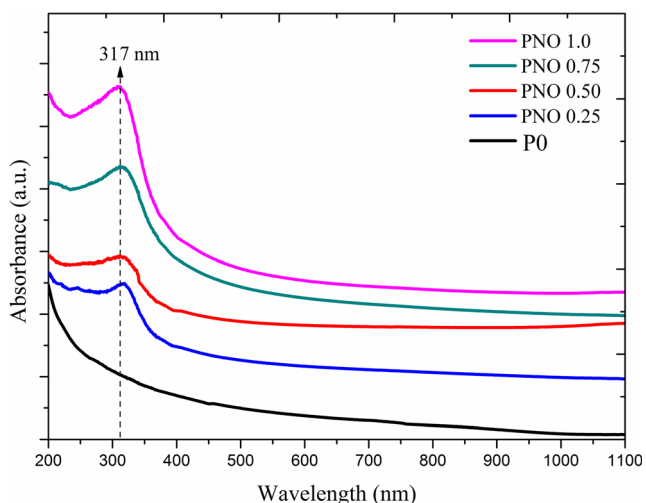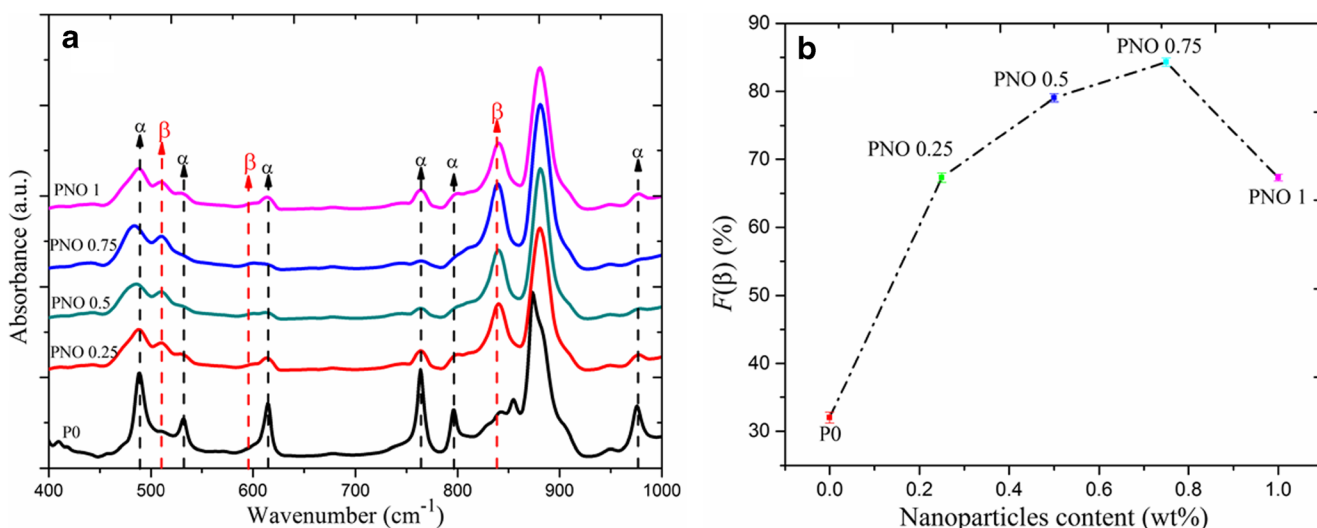

Fig. 6 UV-Visible absorption results of neat PVDF (P0) and the NONPs loaded PVDF films (PNO0.25, PNO0.5, PNO0.75 and PNO1)

Fig. 7 (**a**) FTIR spectra of the P0 and NONPs loaded PVDF films (PNO0.25, PNO0.5, PNO0.75 and PNO1). Dotted red and black lines are corresponding to the β phase and α phase PVDF respectively; (**b**) Variation of β phase fraction (F(β)) with NONPs loading in PVDF matrix

temperature range is observed for the sample PNO0.75 in comparison with the neat PVDF. This increase in the melting temperature is ascribed to the change in degree of crystallinity and homogeneity in sub-molecular structure of the nanocomposite film, hence supports the formation of the electroactive β phase in the nanocomposite films [20, 26]. But with further increment of the nanoparticles in PVDF matrix (for PNO1) the melting temperature is decreased. This phenomenon may be occurred due to the agglomeration of the NONPs in the PVDF at higher loading fraction. The decomposition temperature also enhanced for the nanocomposite films in comparison to the neat PVDF films, which infers the good thermal stability of the nanocomposite films. The TGA analysis of the neat and NONPs loaded nanocomposite films is shown in Fig. 8b. A step like weight loss starts around 450 °C and continues up to 500 °C for all the samples. The decomposition of the films is occurred during this weight loss by chain stripping mechanism, through which hydrogen fluoride (HF) gas released. To determine the physical properties of the nanocomposite films interfacial area between the polymer and nanofillers plays a vital role. The nanofiller/polymer interface region (m_I) of the NONPs/PVDF composite films was obtained from the TGA results by using the following Eq. [38],

$$m_I = \frac{m(x)_{I0} - m_{I0}}{m_{I0}} \times 100\% \tag{6}$$

where, m_{I0} is the mass of the neat PVDF at the temperature at which the mass loss rate is maximum and $m(x)_{I0}$ is the mass of the composite containing a given wt% of nanoparticles that has not degraded at the same temperature. The variation of m_I with the loading fraction (0–1%) of the NONPs nanofiller in PVDF is shown in Fig. 9. From this figure it can be seen that the value of m_I is increased with the increasing loading

fraction of the NONPs. The maximum value (19.2%) of m_I is obtained for the sample PNO0.75 which infers that the number of particles interacting with the polymer matrix is highest for PNO0.75. However the value of m_I is decreased for further loading of NONPs in PVDF i.e. for PNO1, which occurred due to the agglomeration of the nanoparticles in the polymer matrix.

Crystallization properties and polymorphism of the neat and nanocomposite films are studied by DSC analysis. DSC heating cycles of the samples P0, PNO0.25, PNO0.75 and PNO1 are shown in Fig. 10a-d respectively. Coexistence of different phases in the samples are analyzed by fitting the DSC curves with multiple Gaussian functions corresponding to the α, β and γ phase PVDF. The fitted curves show three distinguishable peaks which are assigned to the melting temperatures of the samples corresponding to the three different phases (α, β and γ) of the samples. Figure show that with the increasing concentration of NONPs (upto 0.75 wt%) the relative intensity and the area under the peak related to the melting temperature of β phase increases and those of the α phase decreases. This phenomena infers that with the loading of the NONPs in PVDF matrix the phase transformation is occurred from α to β phase of PVDF. Fig. 11 shows the DSC cooling cycle for neat and NONPs loaded PVDF films. It is evident from the figure that crystallization temperature (T_c) corresponding to the single exothermic peak increases with increasing content of NONPs in the PVDF matrix. The crystallization temperature is increased by ~ 3 °C for the sample PNO0.75 in comparison to that of the neat PVDF. This phenomena is occurred due to the presence of NONPs nucleating agents in PVDF matrix, which acts as nucleating centres and accelerate nucleation kinetics. Faster nucleation kinetics for the sample PNO0.75 is also evident from its FESEM image in Fig. 5b which shows formation of comparatively
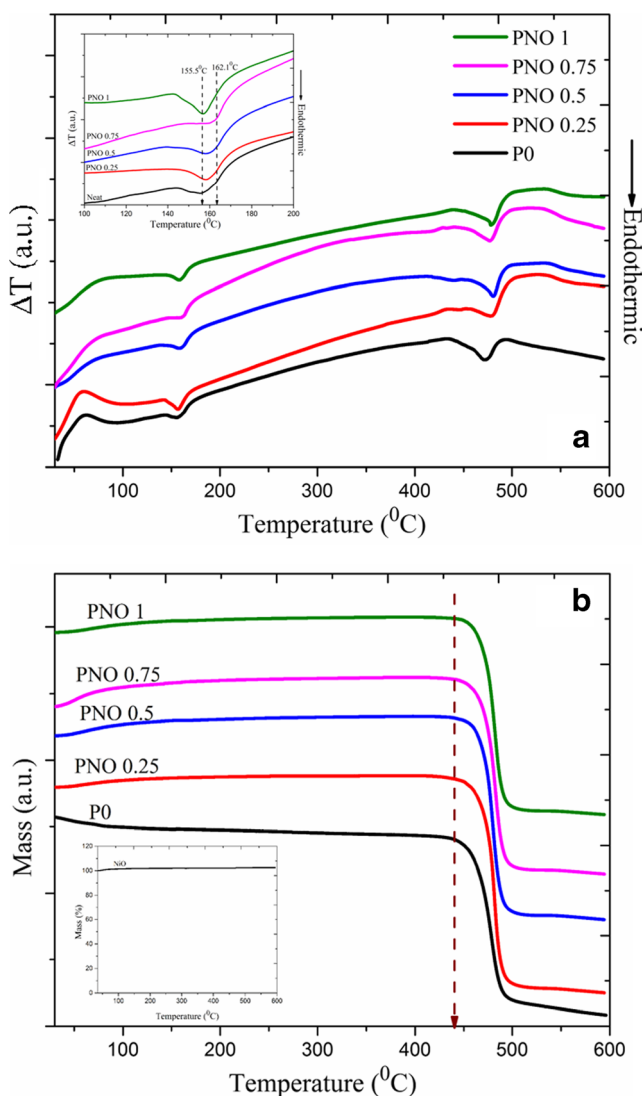
Fig. 9 Variation of nanoparticle/polymer interface (m_I) with NONPs content

Fig. 8 (**a**) DTA of the samples P0, PNO0.25, PNO0.5, PNO0.75 and PNO1. Inset shows enlarged view of the DTA curve in the temperature range 100–200 °C; (**b**) TGA thermographs of the samples P0, PNO0.25, PNO0.5, PNO0.75 and PNO1. Inset shows the TGA thermographs of the synthesized nickel oxide nanoparticles

smaller spherulite due to the addition of NONPs. DSC results are also used to get the enthalpy of crystallization (ΔH_c J/g) and the degree of crystallinity (X_c) of the neat PVDF and NONPs/PVDF composites films. The degree of crystallinity of the samples is calculated by using the Eq. (2) and the variation of X_c with nanofiller content is shown in Fig. 12. Crystallization temperatures (T_c) and enthalpy of crystallization (ΔH_c) for the neat PVDF and nanocomposite films are given in Table 2. With the incorporation of the NONPs in PVDF matrix crystallinity decreases and for the sample PNO0.75 the value of X_c is minimum.

Mechanism of electroactive β phase nucleation XRD, FTIR and thermal studies of the nanocomposite films confirms that the incorporati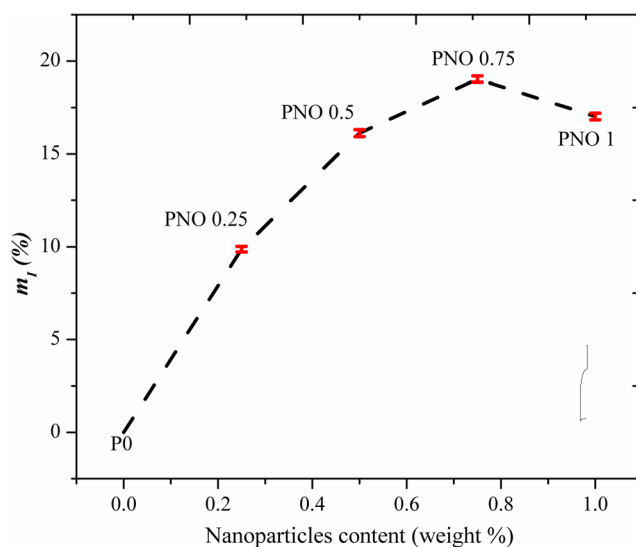on of nickel oxide nanoparticles in the PVDF matrix promotes the increment of the electroactive β phase nucleation. Therefore it is important to analyze the interaction between the nickel oxide nanoparticles and the polymer matrix. The strong interactions between the PVDF matrix and incorporated nanoparticles may be responsible for the improvement of electroactive β- phase fraction in PVDF [20, 24]. During the synthesis of nickel oxide nanoparticles, the pH of the nickel precursor solution was maintained at 13 by using NaOH solution. The variation of the Zeta potential of the nickel oxide nanoparticles with pH for the respective precursor solution was reported by L. Xiang et al. [32], where the value of the Zeta potential at pH 13 confirms the presence of negatively charged surface of the synthesized nickel oxide nanoparticles. When this negatively charged nanoparticles are added to the PVDF matrix in the solution phase, the nanoparticles act as the substrate for the formation of electroactive β phase. There is a strong electrostatic interaction between the partially positive –CH_2 dipoles and the negatively charged nanoparticle surfaces, that leads to the alignment of the stabilized PVDF chains on the surface of the nanoparticles in a longer 'all-trans' (TTT) conformation resulting the formation of electroactive β phase [33–35]. Hence the negatively charged surfaces of the nanoparticles act as the nucleation centers for the formation of the electroactive β phase. Fig. 13 represents the schematic of the ion-dipole interaction mechanism between the nanoparticles and the polymer chains. It is worthy to mention here that a small fraction of the electroactive γ phase of PVDF has been found for the PVDF composite films in our work. Similar results for PVDF/ NaY zeolite and PVDF/ clay composites was previously reported by A.C. Lopes et al. [36, 37]. According to their work γ phase formation may be originated due to the gauge effect which is the result of easier local internal chain rotation.
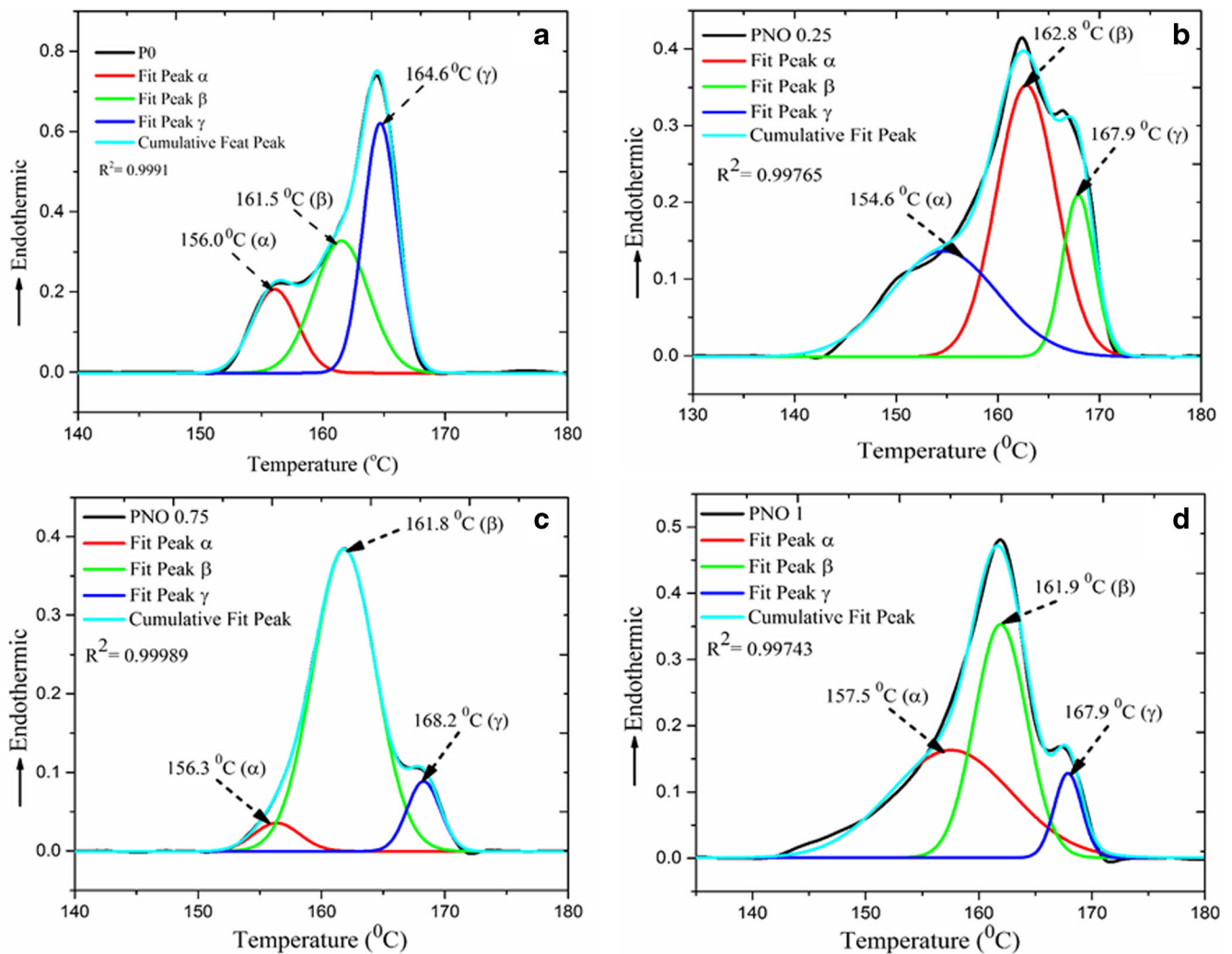
Fig. 10 DSC heating cycles for the samples (**a**) P0; (**b**) PNO0.25; (**c**) PNO0.75; (**d**) PNO1. DSC curves are fitted with multiple Gaussian functions corresponding to the α, β and γ phase PVDF

Dielectric properties

(a) Dependence of dielectric properties on NPs content
Fig. 14a shows the variation of dielectric constant and dielectric loss at 100 Hz of the NiO nanoparticles loaded PVDF films with the variation of NPs content. The dielectric constant increases with the increment of loading fraction of the NiO nanoparticles in the polymer matrix up to 0.75 wt% and decreases for higher loading content. Maximum value of dielectric constant c.a. 32 is obtained at 0.75 wt% NONPs loading (PNO0.75). Fig. 14b shows the dependence of ac conductivity of the samples on NONPs loading fractions at 100 Hz. An increment in calculated ac conductivity value with NONPs content has been observed up to 0.75 wt% and then it decreases for higher loading fraction of NPs in PVDF. The enhancement of dielectric properties can be readily explained by two major phenomena. First one is the Maxwell–

Wagner–Sillars (MWS) interfacial polarization effect which appears for heterogeneous medium consisting of different phases having dissimilar permittivity and conductivity; and this effect causes accumulation of the charges at the interfaces [22, 24]. With an increase in NPs content, the number of NPs and total interfacial area per unit volume are increased while the inter-particle distance are decreased. This improves the average polarization associated with the NPs and the coupling between neighboring grains of polymer resulting in the enhanced dielectric constant of the nanocomposite films. Agglomeration of the NPs at higher concentration (above 0.75 wt% loading) leads to decrease in the interfacial area per unit volume resulting less value of dielectric constant and ac conductivity [22, 24]. The other responsible phenomenon is the enhancement of electroactive β phase content in the polymer nanocomposite films by introducing NONPs in PVDF matrix, due to which the dielectric
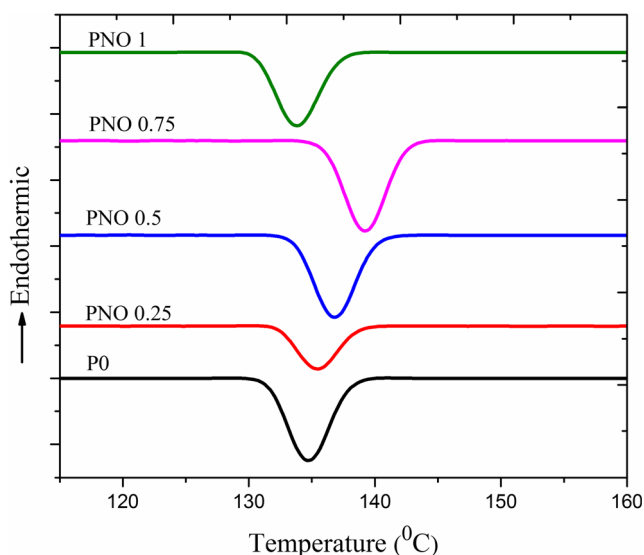
Fig. 11 DSC cooling cycle for the samples P0, PNO0.25, PNO0.5, PNO0.75 and PNO1

Fig. 12 Variation of degree of crystallinity ($X_c\%$) with nickel oxide nanofiller content

property of the nanocomposites samples is also enhanced. In β phase, strong dipolar interaction between the negatively charged NPs surfaces and the –CH₂ dipoles of PVDF partially contributes to the high dielectric properties of NONPs loaded PVDF thin films. Thakur et al. [27] reported similar type work where the highest value of dielectric constant was obtained about 29 for 15 wt% nickel oxide/PVDF composites. But in this work, only 0.75 wt% NONPs loading in PVDF matrix results dielectric constant of 32. This comparatively higher value of dielectric constant at lower filler concentration is achieved due to the more homogeneous and discrete distribution of the smaller sized NiO particles in PVDF matrix. To have a detail idea about the dependence of the dielectric constant of the NONPs/PVDF composite films on the filler concentration a series-parallel model was employed [21], which is as follows:

$$\varepsilon_r{}^s = (1-v)\varepsilon_p{}^s + v\varepsilon_f{}^s, \quad s \in [-1, 1], \tag{7}$$

where, ε_r, ε_p, and ε_f are the relative permittivity of NONPs/PVDF composite film, neat PVDF matrix, and NONPs filler respectively. Here, $v = cv_f$ ($v_f + v_p = 1$) v_p and v_f are the volume fraction of the PVDF matrix and NONPs, c is a constant and s is the depolarization factor. In this model each filler/polymer grain can be deemed as unit. As shown in the Fig. 14c the experimental values of ε_r (at 100 Hz) are well fitted with the series-parallel model which infers that the NiO nanofillers are not in conducting phase. The experimentally measured value of ε_f c.a. 570 was used during the curve fitting.
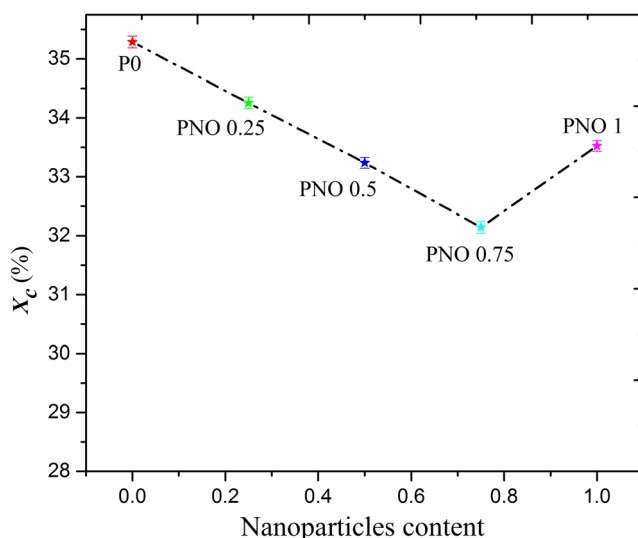
(b) Frequency dependence of the dielectric properties
Fig. 15a shows the frequency dependent dielectric properties of the NONPs loaded PVDF films at room temperature and atmospheric pressure. The dielectric constant (ε_r) decreases with increasing frequencies for neat as well as nanocomposite films. This phenomenon is occurred due to the decrease in number of aligned dipoles with increasing frequency [22]. When the frequency is low ($\omega << 1/\tau$), where τ is the relaxation time, the orientation of the dipoles can follow the field but when the frequency of the external field increases ($\omega < 1/\tau$), the dipoles begin to lag with the field. At high frequency region ($\omega >> 1/\tau$), the dipoles can no longer follow the electric field and the dielectric constant decreases. The decrease in dielectric constant with frequency can also be explained by the MWS interfacial polarization mechanism [22, 24]. When an electric field is applied, the space charge accumulation and short-range dipole–dipole interactions at the interfaces of the NONPs/PVDF result in large interfacial polarization as well as large dielectric constant at lower frequencies. But with the increasing frequencies the interfacial

Table 2 Crystallization temperature (T_c) and enthalpy of fusion (ΔH_c) of the neat and NONPs loaded PVDF films

Sample Name	Crystallization temperature (T_c)(°C)	Enthalpy (ΔH_c)
P0	134.7	36.9
PNO0.25	135.5	35.82
PNO0.75	139.2	33.62
PNO1	133.8	35.06

Fig. 13 Schematic of β phase
formation mechanism
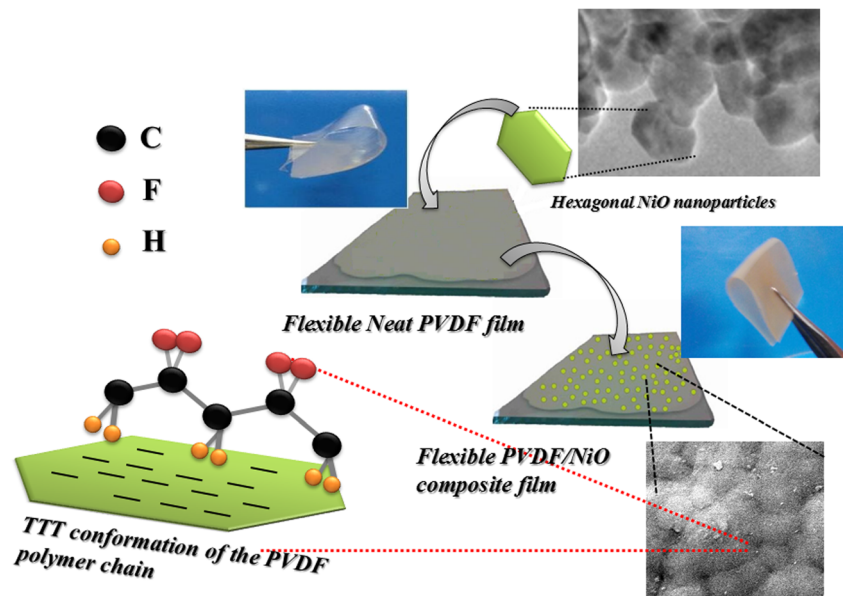
polarization in nanocomposite films decreases may be due to the confinement of charge carriers in the samples. At 20 Hz dielectric constant of value 37.6 is achieved for 0.75 wt% of NONPs /PVDF nanocomposites (Fig. 15a), which is about 4 times greater than that of the neat PVDF film. Fig. 15b shows the frequency dependence dielectric loss (ε) of the neat and nanocomposite films. It can be clearly seen from the figure that the dielectric loss increases with the loading of the NONPs and at 20 Hz the corresponding value is ~3.85 for PNO0.75. Fig. 15c shows the frequency dependence of ac conductivity of the NONPs loaded PVDF films. The conductivity of the samples may be divided into two different frequency regions. At the low frequency region the conductivity is mainly dominated by dc conductivity and at higher frequencies it is frequency dependent conductivity i.e. ac conductivity. The variation of the ac conductivity with frequency also follows the MWS interfacial polarization effects and dielectric relaxations [22, 24]. Therefore the ac conductivity increases with increasing frequencies for all the samples. At 20 Hz the highest ac conductivity is observed for PNO0.75 (9.5×10^{-5} Sm^{-1}).

Ferroelectric properties The effect of NONPs loading on ferroelectric behavior of PVDF composites can be studied through P-E hysteresis measurement at a particular temperature and frequency. Fig. 16 shows the polarization (P) vs. the applied electrical field (E) curve which is generally referred as P-E curve. Figure depicts the P-E curves for the neat and PNO0.75 film. Phase difference

between the charge and voltage signals is produced while energy is dissipated by a material. This phase difference produces a loop with a definable area under the curve which refers the charge storing capability of the material. In an ideal ferroelectric polymer, the polarization due to the molecular dipoles are responsible for the charge accumulation. However, in a dielectric composite material, interfacial polarization occurs due to the accumulation of charges at the interfaces of the heterogeneous material [38, 39]. As the NONPs is more conductive than the polymer, that results the restricted charge mobilization within the particles/polymer interface. This restricted mobilization of charges facilitates the hetero-polarization in the material [38, 39]. The neat and PNO0.75 films were subjected to a 700 KV/m electric field to measure polarization. The 0.75 wt% NiO / PVDF film was chosen because maximum (85%) β phase was achieved at this loading fraction. The dimensions of the film were kept constant in all cases. Carbon tape was used as the upper and lower electrodes. The area of the electrodes was around 8.4×10^{-3} m^2, and the thickness of the films was 300 μm. The area of the PE hysteresis loops are 6.72 and 40.60 J/m^3 for neat and PNO0.75 respectively as calculated from the PE curves shown in Fig. 16. This increment in area of PE hysteresis loop infers more charge storing capability of the PNO0.75 than the neat PVDF, which supports the enhanced dielectric value. The values of remnant polarizations were obtained as 9.8 and 46.0 μC/m^2 for P0 and PNO0.75 respectively. The value of remnant polarization is increased in PNO0.75 due to the hetero-polarization, as well as formation of the β phase. The remnant polarization is directly proportional
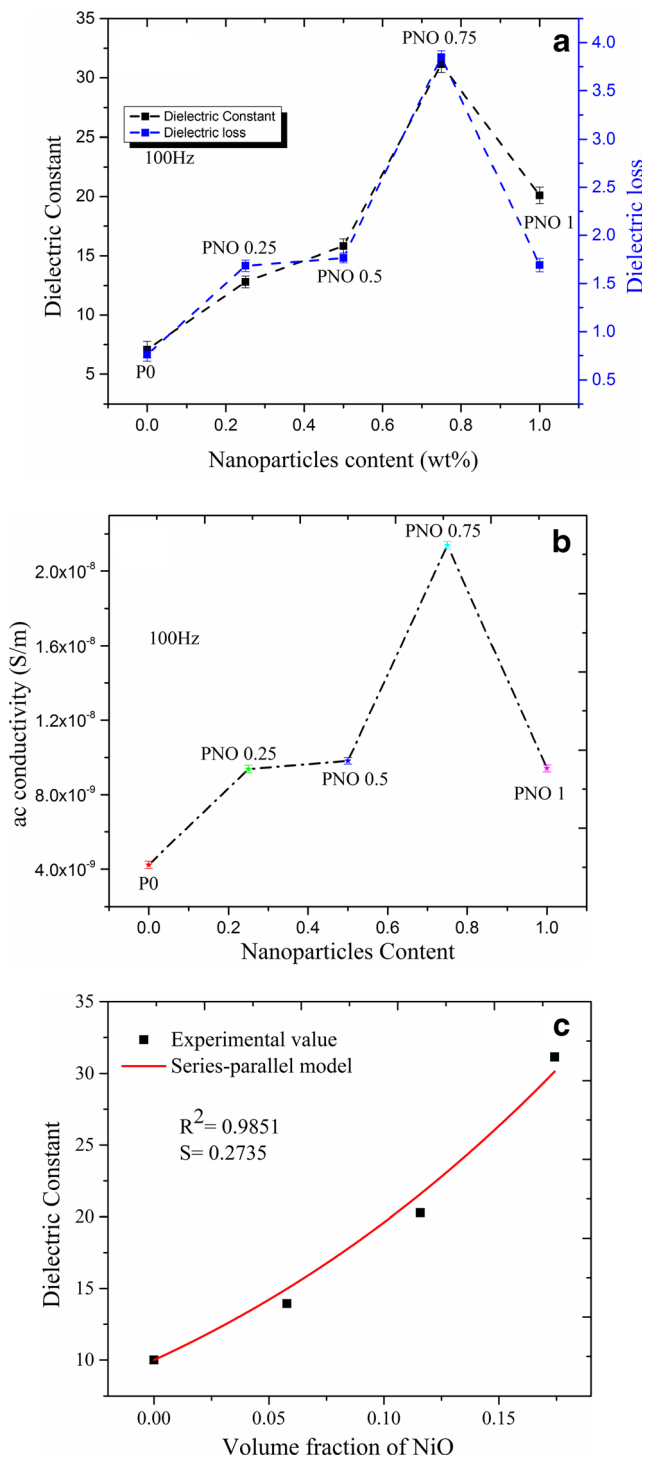
Fig. 14 (a) Variation of dielectric constant and dielectric loss with loading concentration at 100 Hz; (b) Variation of ac conductivity with loading concentration at 100 Hz; (c) fitted dielectric constant (at 100 Hz) vs volume fraction of the nickel oxide nanopartricles filler
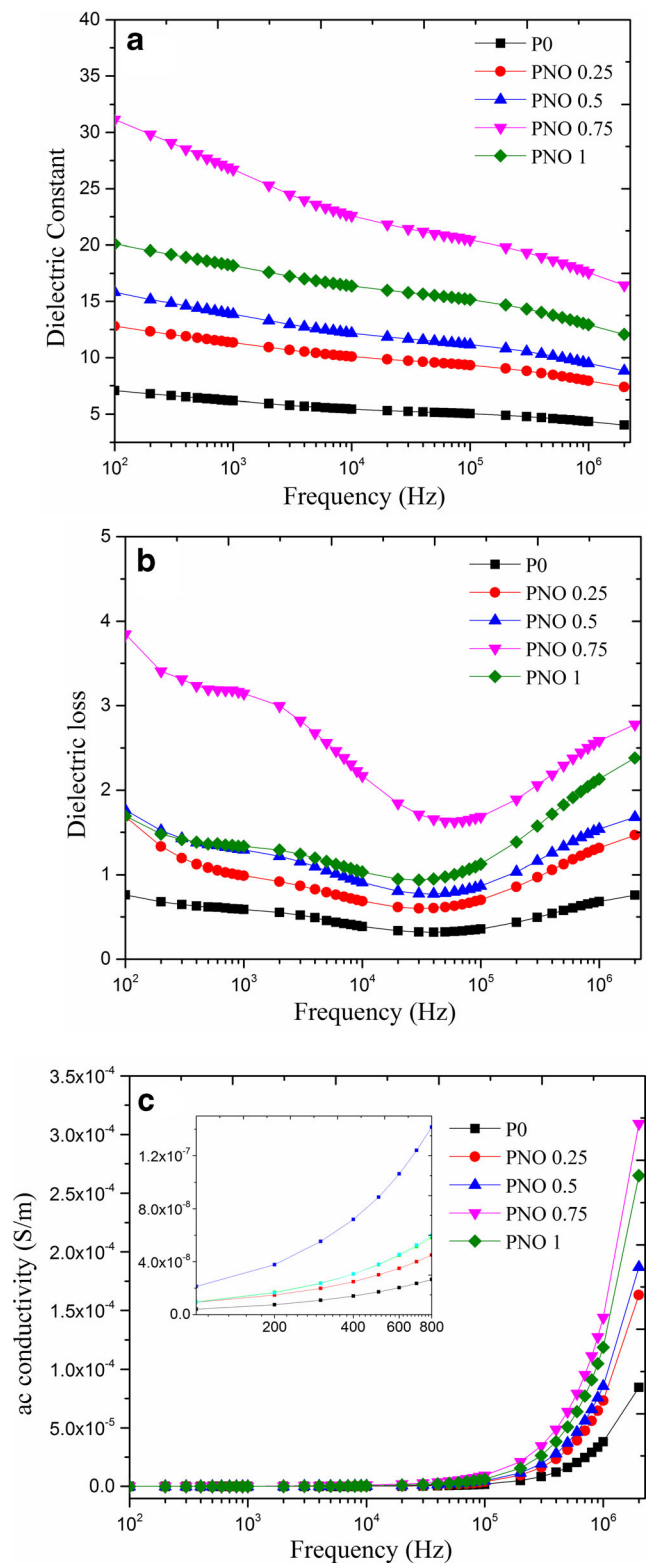
Fig. 15 Variation of (a) dielectric constant (ε_r); (b) dielectric loss (ε); (c) ac conductivity with frequency of the samples P0, PNO0.25, PNO0.5, PNO0.75 and PNO1

to the piezoelectric response of the material [39, 40]. The coercive field of the PNO0.75 is also increased to 125 KV/m. As the remnant polarization and coercive field of PNO0.75 is much higher than that of neat PVDF, hence

the power generating capability of PNO0.75 is also higher than that of neat PVDF.
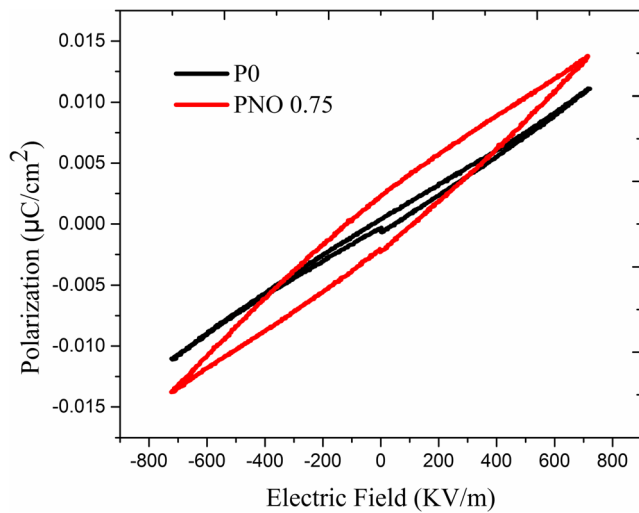
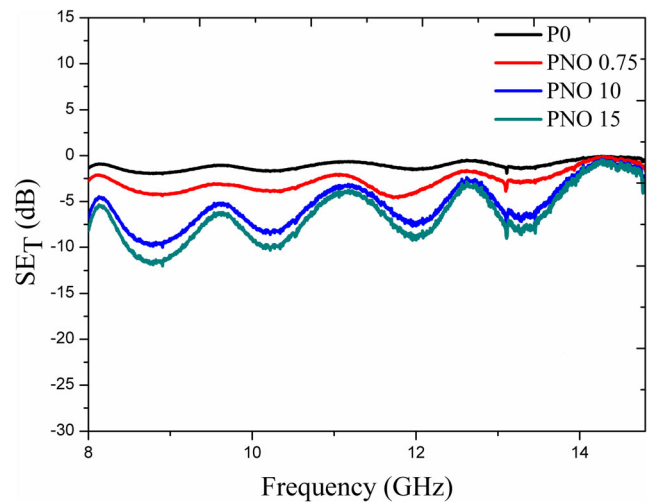Fig. 16 P-E hysteresis loop for the samples P0 and PNO0.75

Fig. 17 Variation of Total EMI shielding effectiveness (SE$_T$) with frequency for the samples P0, PNO0.75, PNO10 and PNO15

EMI shielding Attenuation of the electromagnetic waves by a materials is called electromagnetic interference (EMI) shielding. When the EM wave is propagating through a shielding medium the attenuation can be occurred via two major paths, reflection loss and absorption loss. Total EMI shielding (SE$_T$) is the combined effect of reflection shielding effectiveness (SE$_R$) and absorption shielding effectiveness (SE$_A$). Through induced conduction current, the electric field associated with EM radiation interacts with free electrons and leads to the EM wave shielding by reflection loss. On the other hand attenuation by absorption loss is important for the shielding materials having high permeability and permittivity due to the strong interaction of EM wave with the electric or magnetic dipoles. For shield materials having thickness higher than Skin depth, the effect of multiple reflection of GHz range EM wave is not considered separately [6]. For sufficiently thick shield material, multiple reflected waves from different internal surfaces and interfaces of the shield material are absorbed internally and absorption component of shielding (SE$_A$) is increased instead of multiple reflection [41]. Considering the effective power of the incident electromagnetic wave inside the shield material the SE$_R$, SE$_A$ and SE$_T$ can be conveniently expressed as [3–5],

$$SE_R = 10 log_{10}\left(1-S_{11}^2\right), SE_A = 10 log_{10}\left(\frac{S_{21}^2}{1-S_{11}^2}\right), SE_T$$

$$= SE_R + SE_A = 10 log_{10}\left(\frac{1}{|S_{21}|^2}\right) \quad (8)$$

Total EMI shielding effectiveness (SE$_T$) of neat PVDF as well as nickel oxide nanoparticles loaded PVDF nanocomposites films in X-band frequency region (8.2–12.4 GHz) is shown in Fig. 17. Neat PVDF film is almost transparent in X-band radiation. The value of SE$_T$ of the NONPs/PVDF nanocomposites films increases with the increasing NiO nanoparticles filler loading as shown in the Fig. 17 which shows SE$_T$ value of 10–12 dB at 15 wt% NiO nanoparticles loading. R. Bera et al. reported that the 3 wt% multiwall carbon nanotube (MWCNT) incorporated polycarbonate/poly (vinylidene) exhibits SE$_T$ value 14–22 dB in 8–18 GHz frequency region, and the thickness of the sample was 5 mm which is quite thick for that study [42]. Enhancement of EMI shielding efficiency with less film thickness and good flexibility is most desirable for useful applications. In this study the thickness of all the nanocomposites films was only ∼ 300 μm and it is capable to block EM radiation prominently in X-band radiation. Well dispersed NONPs in the polymer matrix cause the increased interfacial area between filler and polymer which leads to the improvement of SE$_T$ value. In this work we have reported the EMI Shielding measurement up to 15 wt% loading of NONPS in PVDF matrix. After 15 wt% loading of the filler concentration the EMI Shielding efficiency is reduced, which may be due to agglomeration of the NONPs loading to less effective interfacial area between polymer matrix and filler. For the sample PNO15 the calculated value of absorptivity (A = 1-S_{11}^2-S_{21}^2) is two times higher than that of reflectivity (R=$\left|S_{11}^2\right|$) at 8.9 GHz. Therefore shielding by absorption is the dominating phenomena at this frequency range. Hence low cost NiO/PVDF nanocomposite films with good flexibility, less thickness, and good thermal stability, can be potentially used in EMI shielding technology.

Table 3 Comparison of the different properties of NiO/PVDF nanocomposites with the other composites

Materials	β phase content	Dielectric properties		Ferroelectric properties	EMI Shielding effectiveness	Reference
		Dielectric constant	Dielectric loss			
0.75 wt% NiO/PVDF	85%	32 at 100 Hz	3.8 at 100 Hz	Remnant polarization 46.0 $\mu C/m^2$ (9.8 $\mu C/m^2$ for neat PVDF)	10–12 dB for X-band at 15 wt% (film thickness ~ 300 μm)	This work
10 mass% NiO/PVDF	82%	27 at 100 Hz	6.7 at 100 Hz	—	—	[27]
50 wt% NiFe$_2$O$_4$/ PVDF	87%	20 at 1KHz	3.8 at 1KHz	—	—	[43]
5 wt% CoFe$_2$O$_4$/PVDF	75%	12 at 100 Hz	1.1 at 100 Hz	Remnant polarization 0.455 $\mu C/cm^2$ (0.345 $\mu C/cm^2$ for neat PVDF)	—	[44]
10 wt% MgFe$_2$O$_4$/PVDF	Increment mentioned but value was not calculated	7 at 1KHz	0.7 at 1KHz	—	—	[45]

Conclusion

In this work, a series of self-standing, flexible NONPs/PVDF composite films were synthesized by a simple solution casting technique and the effect of NONPs on the enhancement of dielectric, piezoelectric and ferroelectric properties of PVDF is rigorously studied. The hexagonal nickel oxide nanoparticles having average size about 44 nm were synthesized by the modified hydrothermal method. This work discloses that the electroactive β phase fraction in PVDF increases with increasing NONPs loading in PVDF matrix up to a critical filler loading (0.75 wt%). PNO 0.75 shows highest β phase fraction about 85%. The enhancement in β phase fraction of PVDF is attributed to the interaction of the negatively charged nanoparticles surfaces and the positive –CH$_2$ group of the PVDF polymer chain, which leads to the alignment of the stabilized, longer 'all-trans' (TTT) conformation of PVDF chain on the surface of the nanoparticles resulting in the nucleation of electroactive β phase. At the critical filler loading fraction a notable improvement in dielectric constant with less dielectric loss is evident in this work. The obtained values of dielectric constant and loss of PNO 0.75 at 100 Hz are 32 and 3.8 respectively. The composite films with critical filler loading can sustain a high dielectric constant value c.a. 18 even at a high frequency 1 MHz. Dielectric property of the composites was well described by the series-parallel model, which infers the nonconducting nature of the nanofillers. Ferroelectric property of the composites is also considerably improved, where area of the hysteresis loop for the sample PNO 0.75 is increased to 40.6 J/m^3 and remnant polarization becomes 46 μC/m^2. It should be noted that the enhancement in the remnant polarization is directly related to the enhancement of piezoelectric response of the composites material. Improvement of these properties is mainly attributed to the discrete distribution of NiO nanoparticles in the PVDF matrix. Due to the selective dispersion, high interfacial area between the non-agglomerated NiO nanofiller and polymer is achieved, hence causes intimate interaction between nanofiller and polymer. The calculated nanoparticles/polymer interface is maximum for PNO 0.75 (19.2%), this indicates that the NONPs are nicely dispersed in PVDF matrix up to 0.75 wt% loading. EMI shielding properties of the NONPs/ PVDF composites films was also investigated above the critical filler loading (>0.75 wt%) where NONPs form interconnected, conductive network in the PVDF matrix. The obtained total EMI shielding value of the 300 μm thick composites films is 12 dB at 8.9 GHz for 15 wt% NONPs loading. Table 3 shows comparison of different properties of NiO/ PVDF nanocomposites with the same of other related composites, which proves the better figure of merits of our nanocomposites irrespective of any of the properties [43–45]. Hence this multifunctional nanocomposites, NONPs/PVDF having high flexibility, low density, low thickness, fair thermal

stability shows fair improvement in dielectric, ferroelectric, piezoelectric and EMI shielding properties; consequently it can be potentially used in energy harvesting and EMI shielding technology immediately.

References

1. Gargama H, Thakur AK, Chaturvedi SK (2015). J Appl Phys 117: 224903
2. Pawar SP, Biswas S, Kar P, Bose S (2016). Polymer 84:398–419
3. Sharma M, Singh MP, Srivastava C, Madras G, Bose S (2014). ACS Appl Mater Interface 6:21151–21160
4. Joseph N, Singh SK, Sirugudu RK, Murthy VRK, Ananthakumar S, Sebastian MT (2013). Mater Res Bull 48:1681–1687
5. Lee B-W, Shen Y, Yue Z-X, Nan C-W (2006). AIP Appl Phys Lett 89:132504
6. Biswas S, Kar GP, Bose S (2015). Phys Chem Chem Phys 17: 27698–27712
7. Chang YM, Lee JS, Kim KJ (2007). Solid State Phenom 124:299–302
8. Lovinger AJ (1983). Science 220:1115–1121
9. Fukada E (2000). IEEE Trans Ultrason Ferroelectr Freq Control 47: 1277–1290
10. Salimi A, Yousefi AA (2003). Polym Test 22:699–704
11. Zhang QM, Bharti V, Zhao X (1998). Science 280:2101–2104
12. Bauer S (1996). J Appl Phys 80:5531–5558
13. Zhang QM, Li HF, Poh M, Xu HS, Cheng Z-Y, Xia F, Huang C (2002). Nature 419:284–287
14. Nambiar S, Yeow JTW (2011). Biosens Bioelectron 26:1825–1832
15. Xu P, Ye K, Du M, Liu J, Cheng K, Yin J, Wang G, Cao D (2015). RSC Adv 5:36656–36664
16. Martins P, Silva M, Mendez SL (2015). Nano 7:9457–9461
17. Fang H, Li Q, He W, Li J, Xue Q, Xu C, Zhang L, Ren T, Dong G, Chan HLW, Dai J, Yan Q (2015). Nano 7:17306–17311
18. Yuan Y, Xiao Z, Yang B, Huang J (2014). J Mater Chem A 2:6027–6041
19. Tamang A, Ghosh SK, Garain S, Alam MM, Haeberle J, Henkel K, Schmeisser D, Mandal D (2015). ACS Appl Mater Interfaces 7: 16143–16147
20. Dutta B, Kar E, Bose N, Mukherjee S (2015). RSC Adv 5:105422–105434
21. Zhang C, Chi Q, Dong J, Cui Y, Wang X, Liu L, Lei Q (2016). Sci Rep. https://doi.org/10.1038/srep33508
22. Thakur P, Kool A, Hoque NA, Bagchi B, Das S, Nandy P (2015). RSC Adv 5:28487–28496
23. Thakur P, Kool A, Bagchi B, Das S, Nandy P (2014). Appl Clay Sci 99:149–159
24. Kar E, Bose N, Das S, Mukherjee N, Mukherjee S (2015). Phys Chem Chem Phys 17:22784–22798
25. Mandal D, Henkel K, Schmeißer D (2012). Mater Lett 73:123–125
26. Lebedev SM, Gefle OS, Tkachenko SN (2010). J Electrost 68:122–127
27. Thakur P, Kool A, Hoque NA, Bagchi B, Sepay N, Das S, Nandy P (2016). RSC Adv 6:26288–26299
28. Bose N, Basu M, Mukherjee S (2012). Mater Res Bull 47:1368–1373
29. Martins P, Lopes AC, Lanceros-Mendez S (2014). Prog Polym Sci 39:683–706
30. Salavati-Niasari M, Mir N, Davar F (2010). J Alloys Compd 493: 163–168
31. Sharma M, Madras G, Bose S (2015). Cryst Growth Des 15: 3345–3355
32. Xiang L, Deng XY, Jin Y (2002). Scr Mater 47:219–224
33. Sebastian MS, Larrea A, Gonçalves R, Alejo T, Vilas JL, Sebastian V, Martins P, Lanceros-Mendez S (2016). RSC Adv 6(114): 113007–113015
34. Martins P, Costa CM, Benelmekki M (2012) Gabriela Botelho and Senentxu Lanceros-Mendez. Cryst Eng Comm 14:2807–2811
35. Martins P, Caparros C, Gonçalves R, Martins PM, Benelmekki M, Botelho G, Lanceros-Mendez S (2012). J Phys Chem C 116: 15790–15794
36. Lopes AC, Costa CM, Tavares CJ, Neves IC, Lanceros-Mendez S (2011). J Phys Chem C 115:18076–18082
37. Lopes AC, Caparros C, Gómez Ribelles JL, Neves IC, Lanceros-Mendez S (2012). Microporous Mesoporous Mater 161:98–105
38. Jayakumar OD, Abdelhamid EH, Kothari V, Mandal BP, Rao R, Jagannath, Naik VM, Naik R, Tyagi AK (2015). Dalton Trans 44: 15872–15881
39. Rahman MA, Chung G-S (2013). J Alloys Compd 581:724–730
40. Martins P, Costa CM, Benelmekki M, Botelho G, Lanceros-Me'ndez S (2013). J Mater Sci 48:2681–2689
41. Kar E, Bose N, Dutta B, Mukherjee N, Mukherjee S (2017). Eur Polym J 90:442–455
42. Bera R, Suin S, Maiti S, Shrivastava NK, Khatua BB (2015). J Appl Polym Sci 132:46
43. Martins P, Costa CM, Botelho G, Lanceros-Mendez S, Barandiaran JM, Gutierrez J (2012). Mater Chem Phys 131:698–705
44. Suresh G, Jatav S, Ramachandra Rao MS, Satapathy DK (2017). Mater Res Express 4:075301
45. Revathi V, Dinesh Kumar S, Chithra Lekha P, Subramanian V, Natarajan TS, Muthamizhchelvan C (2014). Acta Metall Sin (English Letters) 27:557–562